



AMERICAN METEOROLOGICAL SOCIETY

Journal of Physical Oceanography

EARLY ONLINE RELEASE

This is a preliminary PDF of the author-produced manuscript that has been peer-reviewed and accepted for publication. Since it is being posted so soon after acceptance, it has not yet been copyedited, formatted, or processed by AMS Publications. This preliminary version of the manuscript may be downloaded, distributed, and cited, but please be aware that there will be visual differences and possibly some content differences between this version and the final published version.

The DOI for this manuscript is doi: 10.1175/JPO-D-15-0177.1

The final published version of this manuscript will replace the preliminary version at the above DOI once it is available.

If you would like to cite this EOR in a separate work, please use the following full citation:

Bishop, S., P. Gent, F. Bryan, A. Thompson, M. Long, and R. Abernathey, 2016: Southern Ocean Overturning Compensation in an Eddy-Resolving Climate Simulation. *J. Phys. Oceanogr.* doi:10.1175/JPO-D-15-0177.1, in press.

© 2016 American Meteorological Society



Southern Ocean Overturning Compensation in an Eddy-Resolving Climate

Simulation

Stuart P. Bishop*

North Carolina State University, Raleigh, North Carolina

Peter R. Gent, Frank O. Bryan

National Center for Atmospheric Research, Boulder, Colorado

Andrew F. Thompson

California Institute of Technology, Pasadena, California

Matthew C. Long

National Center for Atmospheric Research, Boulder, Colorado

Ryan Abernathy

Columbia University, New York, New York

*Corresponding author address: Department of Marine, Earth, and Atmospheric Sciences, North

Carolina State University, Campus Box 8208, Raleigh, NC 27695

E-mail: spbishop@ncsu.edu

ABSTRACT

16 The Southern Ocean's Antarctic Circumpolar Current (ACC) and Merid-
17 ional Overturning Circulation (MOC) response to increasing zonal wind stress
18 is, for the first time, analyzed in a high- resolution (0.1° ocean and 0.25° atmo-
19 sphere) fully-coupled global climate simulation using the Community Earth
20 System Model. Results from a 20-year wind perturbation experiment, where
21 the Southern Hemisphere zonal wind stress is increased by 50% south of 30° S,
22 show only marginal changes in the mean ACC transport through Drake Pas-
23 sage; an increase of 6% (136 to 144 Sv) in the perturbation experiment com-
24 pared with the control. However, the upper and lower circulation cells of the
25 MOC do change. The lower cell is more affected than the upper cell with a
26 maximum increase of 64% versus 39% respectively. Changes in the MOC are
27 directly linked to changes in water mass transformation from shifting surface
28 isopycnals and sea ice melt, giving rise to changes in surface buoyancy forc-
29 ing. The increase in transport of the lower cell leads to upwelling of warm
30 and salty Circumpolar Deep Water and subsequent melting of sea ice sur-
31 rounding Antarctica. The MOC is commonly supposed to be the sum of two
32 opposing components: a wind- and transient-eddy overturning cell. Here, the
33 transient-eddy overturning is virtually unchanged and consistent with a large-
34 scale cancellation of localized regions of both enhancement and suppression
35 of eddy kinetic energy along the mean path of the ACC. However, decompos-
36 ing the time-mean overturning into a time- and zonal-mean component and a
37 standing-eddy component, reveals partial compensation between wind-driven
38 and standing-eddy components of the circulation.

39 **1. Introduction**

40 It is currently estimated that more than 40% of the oceanic uptake of anthropogenic CO₂ takes
41 place south of 40°S (Sallée et al. 2012) and mesoscale eddies play an important role in the up-
42 take (Gnanadesikan et al. 2015). The oceanic uptake over the Southern Ocean is largely governed
43 by the strength of the meridional overturning circulation (MOC) and the location of outcropping
44 isopycnals at the surface (Marshall and Speer 2012; Morrison et al. 2015). Over the past fifty
45 years, Southern Ocean winds have been increasing at a steady rate and have shifted poleward in
46 response to anthropogenic forcing from the Antarctic ozone hole in the lower stratosphere and
47 global climate change (Thompson et al. 2011). Recent work from paleo records suggests that the
48 Southern Ocean winds have been weaker in past climates due to an equatorward shift of the polar
49 Westerlies (Toggweiler 2009) and are currently the strongest they have been in the past thousand
50 years (Abram et al. 2014). Understanding how the strength of the Antarctic Circumpolar Cur-
51 rent (ACC) and MOC respond to changing winds is fundamental to understanding global climate
52 change.

53 The ACC and MOC response to changing surface wind and buoyancy forcing hinges on the
54 response by mesoscale eddies. One hypothesis is that there will be zero change in ACC trans-
55 port with increasing winds. The paradigm is that as winds increase, the ACC transport remains
56 roughly constant, because wind-forced steepening of isopycnals will quickly be brought back to
57 their original state. This is accomplished by down-gradient eddy buoyancy fluxes, generated via
58 baroclinic instability, that draw on the excess available potential energy imparted by the increase
59 in zonal wind stress. Interfacial form stress, which is proportional to the eddy buoyancy fluxes,
60 then transfers this excess wind-driven momentum to the sea floor where it is balanced by bottom
61 form drag (Ward and Hogg 2011). The near independence of the ACC transport (usually through

62 Drake Passage) to changes in the Southern Hemisphere wind stress is commonly referred to as
63 *eddy saturation* (Straub 1993; Munday et al. 2013). Eddy saturation is becoming more widely
64 accepted as limited observations (Firing et al. 2011; Chidichimo et al. 2014; Böning et al. 2008)
65 and modeling efforts (Farneti et al. 2015) see only small trends in ACC transport over multiple
66 decades of increased wind forcing.

67 It is less clear how the Southern Ocean’s zonally-integrated meridional circulation responds to
68 changing winds. Theories suggest that the Southern Ocean MOC is the small residual of a near
69 cancelation of two opposing meridional circulation cells; a clockwise (looking west) wind-driven
70 circulation in the density-latitude plane (equatorward at the surface and poleward at depth) known
71 as the “Deacon Cell” and an eddy-driven cell of opposite sense (Johnson and Bryden 1989; Mar-
72 shall and Radko 2003). The near independence of the MOC to changes in wind stress is referred to
73 as *eddy compensation* because any changes to the wind-driven Deacon Cell will be compensated
74 by the eddy-driven circulation. Crucially, any changes in the MOC must be consistent with surface
75 buoyancy modifications, and thus water mass transformation, related to changes in the wind field.

76 The degree of eddy compensation presently taking place in the Southern Ocean is unknown,
77 but there is observational evidence from satellite altimetry that surface eddy kinetic energy (EKE)
78 has increased in recent decades (Meredith and Hogg 2006; Hogg et al. 2015). Oceanic observa-
79 tions are too sparse to make a direct diagnosis of the MOC so that there is no “true” estimate for
80 models to use as a benchmark. Estimates of the MOC from models that most realistically repre-
81 sent the ocean are instead used as a “true” depiction of the MOC. Recent work by Farneti et al.
82 (2015) and Downes and Hogg (2013) show that there is considerable spread in the strength of
83 the MOC across coarse-resolution (1°) models forced with the Coordinated Ocean-ice Reference
84 Experiments (CORE-II) winds (Large and Yeager 2009) and amongst coupled climate models re-
85 spectively. Climate models rely on an accurate parameterization of mesoscale eddies, which are

86 not routinely resolved in climate models (Gent and McWilliams 1990) (hereafter referred to as
87 GM). Idealized studies show that the MOC response is more sensitive to model resolution than is
88 the ACC transport (Stewart et al. 2014; Morrison and Hogg 2013).

89 To address how the MOC will respond to changing winds, a wide range of model experiments
90 have been performed from idealized eddy-resolving zonally-re-entrant channels to more realistic
91 coarse-resolution global circulation models. Gent (2015) provides an extensive review of the ef-
92 fects of Southern Hemisphere wind changes on the MOC in ocean models. Idealized studies that
93 are eddy resolving show that there is partial eddy compensation, but results are sensitive to sur-
94 face boundary conditions (Abernathy et al. 2011; Wolfe and Cessi 2010). Gent and Danabasoglu
95 (2011) (hereafter referred to as GD11) show that in a realistic coupled climate model, eddy com-
96 pensation is achieved if the GM eddy coefficient is allowed to vary in space and time in response
97 to changes in stratification, which is consistent with idealized studies where EKE increases with
98 winds (Abernathy et al. 2011; Morrison and Hogg 2013). The highest resolution simulations to
99 date to investigate MOC changes due to wind forcing are a Southern hemispheric eddy-permitting
100 model ($1/6^\circ$) (Hallberg and Gnanadesikan 2006) and a global eddy-permitting ($1/4^\circ$) simulation
101 (Treguier et al. 2010). However, both models' are uncoupled to the atmosphere and representation
102 of Southern Ocean mesoscale eddies might be under-resolved, because the first baroclinic defor-
103 mation radius, which is the characteristic spatial length scale of mesoscale eddies and ranges from
104 6–25 km in the Southern Ocean (Smith 2007), requires higher than $1/6^\circ$ resolution south of 30°S
105 (Hallberg 2013).

106 To overcome uncertainty regarding the parameterization and resolution of mesoscale eddies,
107 this study examines the ACC transport and MOC response to changing winds in a new, high-
108 resolution version of the Community Earth System Model (CESM). The experiment is conducted
109 with a fully coupled configuration of CESM with an eddy resolving (0.1°) ocean component and

110 high-resolution (0.25°) atmosphere, which also includes sea ice and land components at the same
111 resolution as the ocean and atmosphere respectively. The increase in resolution compared to a
112 standard CESM simulation at coarse resolution (1° ocean and atmosphere) can be seen from snap
113 shots of sea surface temperature (SST) and sea surface height (SSH) in Fig. 1. When mesoscale
114 eddies are explicitly resolved, there is more filamentary structure and closed contours of SSH.

115 With this high-resolution version of CESM we test the ideas of eddy saturation and eddy com-
116 pensation by running a twenty-year wind perturbation (WP) experiment in which the zonal wind
117 stress in the Southern Ocean south of 30°S is increased by 50%, the same as the PERT1 experi-
118 ment in GD11. This is the highest resolution simulation brought to bear on this problem to date.
119 A challenge of interpreting our results is that a twenty-year perturbation experiment will not have
120 equilibrated in the deep ocean. Other modeling efforts at eddy-permitting resolution (0.25°) have
121 experienced considerable model drift (Treguier et al. 2010). The emphasis of this study is on the
122 transient response of the upper part of the the ACC. However, the deeper ACC comes into play
123 through the momentum budget. With this experiment being the first of its kind at this resolution,
124 it is expected that these caveats will be refined over time. Model drift will be discussed further in
125 the model description section.

126 One of the interesting results of this study is that standing eddies play the dominant role in the
127 response of the MOC to increasing winds compared to transient eddies. Standing eddies were
128 recognized as a major contributor to meridional fluxes in the Southern Ocean by early studies
129 (de Szoeke and Levine 1981; Treguier and McWilliams 1990; Wolff et al. 1991). However, popular
130 theoretical models of the ACC are framed in terms of a “streamwise average,” which follows the
131 meanders of the time-mean current, effectively eliminating the standing component and leaving a
132 balance between a wind-driven Ekman component and a transient eddy component (Marshall et al.
133 1993; Marshall and Radko 2003; Nikurashin and Vallis 2012). Recent studies have re-emphasized

134 the importance of standing eddies for the time-mean meridional flux of heat in the Southern Ocean
135 (Volkov et al. 2010; Bryan et al. 2014) and in the response to wind perturbations (Dufour et al.
136 2012; Viebahn and Eden 2012; Zika et al. 2013b; Thompson and Garabato 2014; Abernathey and
137 Cessi 2014).

138 Finally, we show that differences in surface buoyancy flux are closely tied to changes in the
139 MOC. For example, increased upwelling of cold water can lead to cooler SSTs and consequently
140 a decrease in latent and sensible heat fluxes. As described in the theoretical model of Marshall and
141 Radko (2003), the net upwelling and subduction in and out of the surface layer must be balanced
142 by diabatic processes (air-sea fluxes and mixing) within the surface layer. In an idealized, ocean-
143 only, eddy-resolving model, Abernathey et al. (2011) showed how wind perturbation experiments
144 could lead to different MOC changes depending on the details of the surface buoyancy boundary
145 conditions. Only a coupled climate model, such as the one examined here, can hope to represent
146 the full range of feedbacks which govern the changes in SST, surface buoyancy flux, and MOC in
147 response to a wind perturbation. In Sec. 6, we examine the connection between changes in surface
148 buoyancy flux and changes in overturning through the lens of water mass transformation.

149 The paper is organized as follows. In the section 2 the MOC and its constituents are defined.
150 In section 3 the control and WP experiments using high-resolution CESM are described. Section
151 4 shows the results of the ACC transport and MOC response in the WP experiment compared to
152 the control simulation. Section 5 discusses the importance of the standing component of the mean
153 overturning circulation in the MOC balance. Section 6 makes the connection between water mass
154 modification and changes in the MOC. Lastly, section 7 contains a discussion and the conclusions
155 of our results.

156 2. Meridional Overturning Circulation

157 The Southern Ocean MOC in depth space, referred to here as the Eulerian-mean MOC, is cal-
 158 culated by integrating the meridional velocity, v , zonally and vertically,

$$\psi(y, z) = \overline{\oint \int_z^0 v dz' dx}, \quad (1)$$

159 where x and z are the zonal and vertical coordinates respectively. The overbar indicates a time
 160 average, $\overline{(\)} \equiv \frac{1}{\tau} \int_0^\tau (\) dt$, where τ is the averaging period. This representation of the MOC is
 161 largely made up of the wind-driven Ekman circulation which is well known as the ‘‘Deacon Cell.’’
 162 It was later realized by Döös and Webb (1994) that the Deacon Cell vanishes when the MOC is
 163 calculated vertically in density rather than depth space. The overturning circulation calculated
 164 in density space better represents water mass transport, which is largely along isopycnals in the
 165 ACC interior and consistent with the net overturning resulting from two opposing mechanisms; the
 166 wind-driven circulation of the Deacon Cell and the eddy-driven circulation. The MOC is defined
 167 as

$$\psi_{\text{moc}}(y, \sigma) = \overline{\oint \int_\sigma^{\sigma_s} v h d\sigma' dx}, \quad (2)$$

168 where $h(x, y, \sigma, t) \equiv -\partial \tilde{z} / \partial \sigma$ is the thickness of isopycnal layers, \tilde{z} is the depth of isopycnal
 169 surfaces, and σ_s is the density value at the surface. σ is potential density and in practice σ_2
 170 (potential density referenced to 2000 m depth) is used to calculate the MOC since its vertical
 171 structure tends to have monotonic profiles and is a good representation of the MOC calculated in
 172 neutral density classes (Lee and Coward 2003). As mentioned above, ψ_{moc} can be thought of as
 173 consisting of two opposing cells between the wind-driven overturning circulation, $\overline{\psi}$, and transient
 174 eddy-induced overturning circulation, ψ^* ,

$$\psi_{\text{moc}}(y, \sigma) = \overline{\psi} + \psi^*. \quad (3)$$

175 The time-mean overturning circulation in isopycnal coordinates is defined as

$$\overline{\psi}(y, \sigma) = \oint \int_{\overline{\sigma}}^{\overline{\sigma}_s} \overline{v} \overline{h} d\sigma' dx, \quad (4)$$

176 where $\overline{h}(x, y, \sigma)$ is the time mean thickness of isopycnal layers. The transient-eddy-induced over-
177 turning circulation is then given by the difference between the MOC and time mean streamfunc-
178 tions as

$$\psi^*(y, \sigma) = \psi_{\text{moc}} - \overline{\psi} = \overline{\oint \int_{\sigma}^{\sigma_s} v' h' d\sigma' dx}, \quad (5)$$

179 where the prime indicates a deviation from the time mean.

180 3. Model

181 *a. Control experiment*

182 The model used in this study is a high-resolution version of the CESM (Hurrell et al. 2013),
183 a new generation climate system model that is the successor to the Community Climate System
184 Model version 4 (Gent et al. 2011). Details of the simulation examined are summarized below,
185 but for a more in depth description see Small et al. (2014). The model configuration includes
186 the Community Atmosphere Model version 5 (CAM5) with a spectral element dynamical core,
187 Community Ice Code version 4 (Hunke and Lipscomb 2008), Parallel Ocean Program version 2
188 (POP2), and Community Land Model version 4 (Lawrence et al. 2011). CAM5 was integrated
189 with a horizontal resolution of about 0.25 degrees (specifically the spectral element dynamical
190 core with 120 elements on each face of the cubed sphere, referred to as ne120) and 30 levels in the
191 vertical.

192 The POP2 model has a nominal grid spacing of 0.1 degrees (decreasing from 11 km at the Equa-
193 tor to 2.5 km at high latitudes) on a tripole grid with poles in North America and Asia. The con-
194 figuration is similar to that used in McClean et al. (2011) and Kirtman et al. (2012), except that the

195 number of vertical levels was increased from 42 to 62, with more levels in the main thermocline.
196 The ocean communicated with the coupler, providing updated SST and surface currents and re-
197 ceiving updated surface fluxes, every 6 hours and the atmosphere communicated every 10 minutes.
198 The coupler computes air-sea fluxes using the Large and Yeager (2009) surface layer scheme. The
199 land and sea ice models are on the same grids as the atmosphere and ocean models respectively.
200 POP2 has been shown to produce eddy covariances consistent with observations in the Pacific
201 (Bishop and Bryan 2013) and Southern Ocean (Lenn et al. 2011), and this high-resolution version
202 of CESM through spectral analysis produces mesoscale eddy covariances of SST and geostrophic
203 meridional velocity which are consistent with satellite observations (Abernathey and Wortham
204 2015).

205 Following a 15-year spin up, the model was run for 66 years. We will refer to the last 66 years
206 with model year 1 being equivalent to aggregate simulation year 16. For the current work we will
207 focus on model years 45–66, which are the years when the WP experiment was performed and is
208 described below. This time period was chosen because surface fluxes and ACC transport through
209 Drake Passage had reached equilibrium by model year 45 (Small et al. 2014).

210 *b. Wind Perturbation Experiment*

211 The WP experiment is conducted with the same methodology as the PERT1 experiment in GD11
212 where the Southern Hemisphere zonal wind stress is increased by 50%, but here using CESM
213 rather than CCSM4. The WP experiment is just short of a 21-year simulation, starting from March
214 of model year 45 of the control simulation to the end of model year 65. The WP experiment was
215 conducted by multiplying the zonal wind stress forcing the ocean component by 1.5 south of 35°S,
216 with this factor linearly reducing to 1 to the north between 35° and 25°S and to the south between
217 65° and 70°S. The maximum time and zonal mean Southern Hemisphere wind stress is 41% larger

218 compared with the control for model years 56–66 with an increase of 0.083 N m^{-2} from 0.197 N
219 m^{-2} in the control to 0.280 N m^{-2} in WP (Fig. 2a), which is very close to the maximum wind
220 stress values cited in GD11. The increased zonal wind stress was not used in the bulk formulae to
221 calculate the atmosphere-to-ocean heat and freshwater fluxes, and the increased zonal stress is not
222 felt directly by the atmosphere component.

223 One of the complications of interpreting a perturbation experiment is model drift. As mentioned
224 before, model drift complicated results in lower resolution studies (Treguier et al. 2010). The
225 shortness of our WP experiment was dictated by very high computational costs. As demonstrated
226 in Small et al. (2014) and in Fig. 2b, ACC transport through Drake Passage is in equilibrium in
227 the control, exhibiting mainly interannual variability. After a decade of the WP simulation surface
228 variables reached a new equilibrium, which is demonstrated in surface EKE in Fig. 4 and described
229 in the next section. However, deep variables have not reached a new equilibrium. Fig. 3 shows
230 the monthly-averaged and area-averaged deep ocean temperature for the Southern Ocean in the
231 control and WP. The control deep ocean temperature is in equilibrium, albeit with some decadal
232 variability, but the WP is not. However, it is not clear whether a perturbation of this kind will have
233 reached equilibrium after 1000 years.

234 4. Results

235 *a. Antarctic Circumpolar Current Transport Response*

236 The ACC transport through Drake Passage is shown in Fig. 2b. The mean and standard deviation
237 for the control and WP are $136 \pm 3 \text{ Sv}$ and $144 \pm 6 \text{ Sv}$, respectively. The WP time series has a trend
238 over the first ten years of $23 \text{ Sv decade}^{-1}$ with a small negative trend over the last ten years of -6
239 Sv decade^{-1} . It is not immediately clear why there is a small negative trend over the remaining

240 ten years. The overall WP mean transport only increases by 6% with a 41% increase in the zonal
241 wind stress compared to the control simulation. These results suggest that the ACC transport is
242 largely *eddy saturated*.

243 The area-average surface EKE south of 30°S increased immediately following the change in
244 wind stress and then continued to increase for a period of 10 years, before stabilizing at a value
245 28% higher than the control mean (Fig. 4a). The area-average surface EKE has a linear trend
246 over the first ten years of $26 \text{ cm}^2 \text{ s}^{-2} \text{ decade}^{-1}$, but no trend in the last ten years. However, the
247 spatial distribution of the EKE trends over the first ten years have positive and negative values that
248 are $O(\pm 100) \text{ cm}^2 \text{ s}^{-2} \text{ decade}^{-1}$ (Fig. 4b), resembling the mean EKE difference over the last ten
249 years of the simulation (Fig. 5). Fig. 5 shows that there are both regions of enhancement and
250 suppression of EKE along the mean path of the ACC with increased zonal wind stress. Outside of
251 the Malvinas and the Agulhas return flows, the positive trends are largely in regions where standing
252 meanders of the mean flow occur in the lee of major topographic features, as shown in Thompson
253 and Garabato (2014) and Abernathy and Cessi (2014). Both the ACC transport through Drake
254 Passage and the area-averaged EKE have a linear trend during the first then years of the WP (Fig.
255 2b). Once the area-average EKE reaches an asymptote of $\sim 35 \text{ cm}^2 \text{ s}^{-2}$ above the control mean,
256 the ACC transport adjusts to the elevated EKE. For this reason overturning streamfunctions are
257 calculated for the final 10 years of the WP experiment (model years 56–66) in the next section.

258 The small increase in ACC transport is also reflected in the differences in isopycnal surfaces
259 between simulations (Fig. 6). The differences are largely focused in the upper ocean; in particular
260 the top 100 meters within the mixed layer (Fig. 6b). There are only small changes in the interior
261 (Fig. 6a). The top 100 meters is characterized by an increase in surface density in WP as compared
262 to the control (Fig. 11a,b). There is also lighter (or more buoyant) waters at depth north of 45°S.
263 This represents a surface intensified steepening of isopycnal surfaces, which makes up the increase

264 in the ACC transport. On average the water is more dense with a skewed probability density
265 distribution (Fig. 6c).

266 *b. Meridional Overturning Circulation Response*

267 1) EULERIAN-MEAN MERIDIONAL OVERTURNING CIRCULATION

268 The mean overturning streamfunction is made up of the clockwise (looking west) wind-driven
269 circulation in depth- latitude space, the Deacon Cell, and a weaker counterclockwise circulating
270 lower cell (Fig. 7). As expected with the increased winds in the WP simulation, the Deacon Cell
271 is intensified. The peak values of the Deacon cell are 40.5 Sv and 57.1 Sv in the control and WP
272 respectively (Fig. 7 a,b). The latitude and depth of the maximum values of the Deacon Cell are
273 similar between simulations. The latitude and depth of the maximum value of the Deacon cell in
274 the control simulation is 51.8°S and 607 m respectively (Fig. 7a). In WP they are 51.6°S and 552
275 m respectively (Fig. 7b). The maximum increase in the Deacon Cell between the control and WP
276 is 17 Sv and occurs at 48.3°S and at 830 m depth. This is equivalent to a 41% increase in transport,
277 consistent with a linear relationship with the surface wind stress (Fig. 7c).

278 The lower cell is reduced slightly between the control and WP (Fig 7c). The maximum values
279 of the lower cell circulation are -14.7 Sv and -13.5 Sv in the control and WP respectively. The
280 latitude and depth of the maximum value of the lower cell in the control simulation is 36.9°S and
281 3752 m respectively (Fig 7a). In WP they are 36.6°S and 3752 m respectively (Fig. 7b).

282 2) MERIDIONAL OVERTURNING CIRCULATION

283 The overturning streamfunction in isopycnal coordinates, referred to as the MOC, is estimated in
284 this section for the control and WP experiments. Comparing the diagnosed MOC (Eq. 2) against
285 a schematic of the overturning [Fig. 18 in Farneti et al. (2015)] there are four distinct circulation

286 cells, but there are only two cells that change substantially between our simulations which will be
287 described (Fig. 8a–c). There is a clockwise-rotating (looking west) upper cell centered at 48.1°S
288 and $36.2\sigma_2$ with a maximum of 19.8 Sv in the control (Fig. 8a). The upper cell in WP is centered at
289 48°S and $36.35\sigma_2$ with a maximum of 27.5 Sv (Fig. 8b). The upper cell increased by a maximum
290 of 7.7 Sv, which is a 39% increase over the control (Fig. 8c).

291 There is a counter-clockwise-rotating cell called the lower cell that has an enhanced poleward
292 region with a maximum of -20 Sv at 63.5°S and $37.15\sigma_2$ in the control (Fig. 8a). In WP the lower
293 cell has a maximum of -32.7 Sv at 64°S and $37.15\sigma_2$ (Fig. 8b). The counter circulation of the
294 lower cell increased by a maximum of 12.6 Sv in WP compared with the control, which is a 64%
295 increase over the control (Fig. 8c). The lower cell equatorward of 50°S has no difference between
296 simulations (Fig. 8c).

297 One decomposition of the MOC is between the time-mean overturning (Eq. 4) and the transient-
298 eddy-induced overturning (Eq. 5) as stated in Equation 3. The time-mean overturning streamfunc-
299 tion (Fig. 8d–f) has a nearly identical structure of circulation cells to the MOC (Fig. 8a–c). The
300 upper cell has a clockwise circulation with a maximum of 22.3 Sv at 52.2°S and $36.45\sigma_2$ in the
301 control (Fig. 8d). In WP the mean upper cell has a maximum of 30.7 Sv at 48.3°S and $36.30\sigma_2$
302 (Fig. 8e). The difference in the maximum values of the upper cell is 8.4 Sv, which is a 38%
303 increase over the control simulation (Fig. 8f). The lower cell has as a maximum value of -19.6
304 Sv at 64.5°S and $37.15\sigma_2$ in the control (Fig. 8d). In WP it has a maximum value of -30.9 Sv at
305 65.2°S and $37.15\sigma_2$ (Fig. 8e). The lower cell increases by 11.3 Sv, which is 58% greater than the
306 control (Fig. 8f).

307 The transient-eddy-induced streamfunction has a different structure than the MOC or the mean
308 overturning (Fig. 8 g–i). There are two counter circulating cells: an upper and a deep cell. The
309 upper cell is the stronger of the two and has a maximum of -16.7 Sv at 43.7°S and $35.30\sigma_2$ for

310 the control (Fig. 8 g). The upper cell in WP has a maximum of -20.5 Sv at 43.4°S and 35.30 σ_2
 311 (Fig. 8h). The small differences between the two simulations are at most ± 5 Sv concentrated in
 312 the upper cell with virtually no change between the lower cells (Fig. 8i). Overall, the transient
 313 eddy component does not make a large contribution to the zonal-mean overturning, as seen also in
 314 Dufour et al. (2012). However, an analysis in streamwise coordinates (not performed here) would
 315 likely find a much greater role for transient eddies (Viebahn and Eden 2012; Abernathey and Cessi
 316 2014).

317 5. Time-Mean Meridional Overturning Streamfunction

318 In the previous section it was shown that little or no eddy compensation is apparent when the
 319 MOC is decomposed into time-mean and transient components. Much of the change in the MOC
 320 is reflected in the time-mean MOC (Fig. 8c,f). This prompted further investigation into the time-
 321 mean overturning streamfunction. The time-mean overturning circulation, $\overline{\psi}$, can be decomposed
 322 into a time and zonal mean streamfunction, $[\overline{\psi}]$, and a deviation from the zonal mean as the “stand-
 323 ing” component ψ^\dagger ,

$$\overline{\psi} = [\overline{\psi}] + \psi^\dagger. \quad (6)$$

324 $[\overline{\psi}]$ is defined as

$$[\overline{\psi}](y, \sigma) = \oint \int_{[\sigma]}^{[\sigma_s]} [\overline{v}][\overline{h}] d\sigma' dx \quad (7)$$

325 where $[\]$ is a zonal average, $[\] \equiv \frac{1}{L(y)} \oint (\) dx$, and $L(y)$ is the circumpolar length of a given
 326 latitude circle. The residual overturning streamfunction is finally written as the three-part balance

$$\psi_{\text{moc}} = [\overline{\psi}] + \psi^\dagger + \psi^*. \quad (8)$$

327 The time and zonal mean component is essentially the Eulerian-mean MOC (Fig. 7) and
 328 remapped to the time and zonal mean depth of σ_2 surfaces (Fig. 9d-f). The differences in cir-

329 culation cells then are equivalent to the values stated for the Deacon Cell and lower cell in the
 330 subsection 4.b. This decomposition is more physically insightful, because $[\overline{\psi}]$ is directly propor-
 331 tional to the zonal mean Ekman transport and is therefore clearly wind driven.

332 The standing component of the MOC is shown in Fig. 9g–i. Similar to the transient component
 333 it has two counter cells that are comparable in strength: an upper and lower cell. However, the
 334 standing component is stronger than the time and zonal mean component. The upper cell has a
 335 maximum of -39.9 Sv at 51.5°S and 35.8 σ_2 in the control (Fig. 9g). The upper cell in WP has a
 336 maximum of -54.7 Sv at 51.1°S and 35.9 σ_2 (Fig. 9h). The upper cell increased by 14.8 Sv, which
 337 is 37% over the control (Fig. 9i).

338 The lower cell of the standing component has a maximum of -39.1 Sv at 57.8°S and 37.1 σ_2 in
 339 the control (Fig. 9g). In WP the maximum is -61.8 Sv at 57.8°S and 37.12 σ_2 (Fig. 9h). There is a
 340 22.7 Sv increase in the lower cell circulation, which is a 58% increase over the control (Fig. 9i).

341 A large degree of compensation exists between the wind-driven time- and zonal-mean cell and
 342 the standing component of the overturning circulation, even though the peaks in overturning do
 343 not coincide in density-latitude space. In both the control experiment and in response to the wind
 344 perturbation,

$$\delta\psi_{\text{moc}} \approx \delta[\overline{\psi}] + \delta\psi^{\dagger}, \quad (9)$$

345 since the change in transient eddy overturning is negligible, $\delta\psi^* \approx 0$ (Fig. 8i). δ here means
 346 WP minus CNTL. It is interesting to note that the lower cell does not exist in the time and zonal
 347 mean component of the overturning (Fig. 9d,e,f). It is only through the standing component of the
 348 overturning that the lower cell exists in our simulations (Fig. 9g,h,i).

349 The time-mean kinetic energy, $\overline{K} = \frac{1}{2}(\overline{u}^2 + \overline{v}^2)$, is also dominated by the standing component,
 350 which reflects changes in the zonal distribution of kinetic energy. The time-mean kinetic energy is

351 decomposed into a time- and zonal-mean component and a standing component,

$$[\overline{K}] = \underbrace{\frac{1}{2}([\overline{u}]^2 + [\overline{v}]^2)}_{Mean} + \underbrace{\frac{1}{2}([u'^2] + [v'^2])}_{Standing}. \quad (10)$$

352 The biggest changes in the kinetic energy are in the standing component (Fig. 10). The longitu-
353 dinal changes in the velocity field enhances mean kinetic energy as baroclinic eddy growth rates
354 respond to changes in mean stratification and vertical shear (Thompson and Garabato 2014).

355 6. Surface Water Mass Transformation

356 Analysis of changes in the surface water mass transformation is used to better understand the
357 thermodynamics of the changes in the MOC. Here “water mass transformation” refers to the ther-
358 modynamic modification of water density due to diabatic processes such as surface buoyancy
359 fluxes and mixing. When the transformation rates are integrated over isopycnals in an ocean
360 basin, the net transformation must balance the inflow / outflow in density coordinates, i.e. the
361 MOC defined in Eq. 2 (Walín 1982; Tziperman 1986; Speer and Tziperman 1992; Marshall et al.
362 1999; Marsh et al. 2000; Large and Nurser 2001; Judicone et al. 2008; Downes et al. 2011). We
363 can therefore expect the changes in Eq. 2 under wind perturbation to be accompanied by changes
364 in water mass transformation rates.

365 With the wind perturbation there is an indirect effect on the coupled system through changes to
366 the surface properties, and this is reflected in changes to the net surface buoyancy flux (\mathcal{B}). Mean
367 changes in density, SST, and sea-surface salinity (SSS) are shown in Fig. 11. Surface density
368 increases almost uniformly along the ACC, with smaller patches of lighter waters found north of
369 45°S (Fig. 11a). The zonally-averaged density distribution shows that the surface waters are more
370 dense at all latitudes except near 30°S and the increase peaks near 50°S (Fig. 11b). The changes in
371 SST and SSS reflect this increase in density. Water spanning 10–20° latitude surrounding Antarc-

372 tica are warmer and saltier by as much as 1–2°C and 0.25–0.5 g kg⁻¹ respectively (Fig.s 11c,e).
 373 The warmer and saltier waters around Antarctica are mostly density compensated, but density does
 374 increase slightly. Water is cooler throughout most of the Pacific and Indian oceans, but salinity
 375 changes are less prominent with the exception that water is fresher near 30°S in the Pacific. The
 376 zonally-averaged SST and SSS show that the surface waters are more salty at latitudes south of
 377 30° (Fig. 11f), but zonal average SST is only warmer south of 50°S (Fig. 11d).

378 Changes in the surface density field reflect changes to the surface buoyancy flux between the
 379 simulations shown in Fig. 12. Surface buoyancy flux is the sum of surface heat flux (Q_o) and
 380 fresh-water flux (FWF),

$$\mathcal{B} = \frac{\alpha_\theta g}{\rho_o c_p} Q_o - \frac{\alpha_S g}{\rho_{fw}} S_o (E - P - R) \quad (11)$$

381 where $\alpha_\theta = \partial\sigma/\partial\theta$, θ is potential temperature, $\alpha_S = \partial\sigma/\partial S$ and S is salinity, $E - P - R$ is the
 382 surface FWF (evaporation minus precipitation minus runoff), g is the acceleration due to gravity,
 383 $\rho_o = 1026$ is the ocean reference density, $c_p = 3996$ J kg⁻¹ K⁻¹ is the specific heat at constant
 384 pressure for seawater, $S_o = 34.7$ g kg⁻¹ is the ocean reference salinity for the virtual salt flux, and
 385 $\rho_{fw} = 1000$ kg m⁻³ is the density of fresh water. The change in \mathcal{B} shows a complex spatial pattern
 386 with a net buoyancy flux reduction near the coast of Antarctica and along the southern fringes of
 387 the subtropical gyres. Along the core of the ACC, patches of both increased and decreased surface
 388 buoyancy flux occur (Fig. 12a). The sign convention is such that of negative buoyancy flux means
 389 the ocean is either cooling or becoming saltier. The zonally-averaged \mathcal{B} has sinusoidal meridional
 390 structure (Fig. 12b). The changes in surface heat flux (Fig. 12c) dominate changes in surface
 391 buoyancy forcing compared with FWFs (Fig. 12e). The FWF spatial difference (Fig. 12e) and
 392 zonal average difference (Fig. 12f) both show positive buoyancy forcing near Antarctica. This is
 393 consistent with a reduction in sea ice in the WP simulation (Fig. 13). In austral summer (JFM) and
 394 winter (JAS) there is an overwhelming reduction in sea ice thickness surrounding Antarctica in the

395 WP simulation. Changes in FWFs around Antarctica though are masked by increased surface heat
 396 fluxes.

397 Since the MOC was analyzed in σ_2 coordinates, we use the same coordinate for the water mass
 398 analysis. To calculate the time-mean surface water mass transformation, the surface buoyancy flux
 399 (Eq. 11) is integrated over the surface outcrop area as

$$\Omega(\sigma_2) = \frac{1}{g} \frac{\partial}{\partial \sigma_2} \overline{\int_{\mathcal{A}_{\sigma_2}} \mathcal{B} dA} \quad (12)$$

400 where \mathcal{A}_{σ_2} represents integration over the area south of 30° S with density greater than σ_2 . By
 401 breaking \mathcal{B} into Q_o and FWF components, Ω can be decomposed into transformation due to Q_o
 402 (Ω_{HF}) and FWF (Ω_{FWF}). There are additional contributions to water mass transformation due to
 403 interior mixing and cabbeling, but those are not diagnosed here (the necessary model output was
 404 not saved). As shown below, changes in surface transformation can explain most of the changes
 405 in the MOC.

406 Fig. 14 shows the annual mean Ω , Ω_{HF} , and Ω_{FWF} for both control and perturbation experi-
 407 ments. Examining the control case first, we see that Ω contains three peaks, each corresponding
 408 with one of the cells of ψ_{moc} described above and shown in Fig. 8. (The transformation rates
 409 should be compared with the MOC at 30° S.) For the densest waters ($36.6 < \sigma_2 < 37.2 \text{ kg m}^{-3}$)
 410 surface cooling make water denser, with a peak transformation rate of 14 Sv; this corresponds
 411 with the lower cell of the MOC. For water of intermediate density ($35.4 < \sigma_2 < 36.6 \text{ kg m}^{-3}$),
 412 a combination of heat and FWFs (the dominant component) makes the water lighter, with a peak
 413 transformation rate of -32 Sv; this corresponds with the upper cell of the MOC. Ω and ψ_{moc} do
 414 not match up perfectly, since we have not calculated the transformation due to mixing; however,
 415 this component can be inferred as the residual, as shown in Newsom et al. (2015). Mixing causes

416 additional water to be entrained into the subpolar cell; in contrast, mixing weakens the upper cell
417 slightly and redistributes its position in density space.

418 The WP experiment produced a strengthening of both the upper and subpolar MOC cells. Corre-
419 spondingly, in Fig. 14 we see that the transformation rates associated with these cells also increase
420 in magnitude. The increased heat loss associated with the lower cell causes transformation to
421 nearly double for water denser than $\sigma_2 = 37.0 \text{ kg m}^{-3}$, to a maximum of 26 Sv, matching the 12
422 Sv increase in overturning almost exactly. Although the upper cell transformation is dominated
423 by FWFs in the control, it is the heat fluxes which change most strongly under the WP; increased
424 density gain due to surface heat flux strengthens the upper-cell transformation to nearly -40 Sv and
425 shifts its maximum from $\sigma_2 = 36.0 \text{ kg m}^{-3}$ to $\sigma_2 = 36.2 \text{ kg m}^{-3}$, again consistent with the 8 Sv
426 increase in the upper cell. Changes in transformation due to FWF changes were minimal, as also
427 found by Newsom et al. (2015) in a greenhouse-warming scenario.

428 The changes in transformation are driven by the changes in heat flux shown in Fig. 12, namely
429 increased heat flux into the ocean in the ACC latitudes and increased heat flux out of the ocean
430 near Antarctica. The physical explanation for this change is consistent with increased Ekman
431 upwelling. In the ACC latitudes, where the water column is stably stratified in temperature, this
432 brings cooler water to the surface and, due to the interactive nature of latent and sensible heat
433 flux, produces increased heat gain. In the subantarctic region, where warmer water lies below
434 the surface, increased upwelling has the opposite effect, producing increased heat loss. Overall,
435 the entire pattern of Southern Ocean circulation and water mass transformation strengthens with
436 increasing winds.

437 7. Discussion and Conclusions

438 The Southern Ocean ACC transport and MOC response to changes in wind forcing in a fully-
439 coupled high-resolution climate model (CESM) are diagnosed. Results from a ~ 21 -year wind
440 perturbation experiment, where the Southern Hemisphere winds were increased by 50%, show
441 that the ACC transport is nearly eddy saturated, but the MOC is not eddy compensated. The
442 ACC transport response through Drake Passage only changes marginally. During the first ten
443 years of the simulation, while the eddies are ramping up, the ACC transport has a linear trend
444 of $23 \text{ Sv decade}^{-1}$ in response to the increased wind forcing. After a decade the eddies have
445 reached an equilibrium state and the ACC transport adjusted to the elevated level of EKE. The
446 overall ACC transport only increased by 6% compared to the control simulation suggesting that
447 the ACC is nearly eddy saturated. Recent studies have pointed to coastal winds near Antarctica
448 as possible drivers of ACC transport variability (Zika et al. 2013a; Langlais et al. 2015), but the
449 time- and zonally-averaged wind in the WP experiment is indistinguishable from the control near
450 the Antarctica coast south of 65°S (Fig. 2). Thus, these potential mechanisms for ACC transport
451 variability are not explored in this paper.

452 The MOC increased in the upper and lower cells by 63% and 39% respectively. When the MOC
453 is decomposed into time-mean and transient-eddy contributions, the eddy-driven overturning does
454 not change much compared to the control. This result is consistent with the mean upper ocean
455 EKE difference (Fig. 5), where EKE is enhanced and suppressed along the mean path of the
456 ACC. The zonally-integrated mean EKE difference sums to near zero, which may help to explain
457 why our transient overturning difference is negligible. EKE is enhanced at choke points along the
458 mean ACC path near major topography and in the Western Boundary Current regions without any
459 systematic shifts in the Southern Ocean SSH fronts.

460 Comparing the MOC results of this study with the same WP experiment (PERT1) performed
461 in the coarse-resolution CCSM4 climate model in GD11, we find a lesser role for transient ed-
462 dies. The biggest changes in the overturning circulation in our high-resolution experiment arises
463 from enhancement of the steady rather than the transient eddy-induced overturning. When the
464 time-mean overturning circulation is decomposed into a time- and zonal-mean and a standing
465 component, the balance of the MOC is approximately between these two components (Eq. 9). As
466 the winds increase, the standing component of the overturning acts to partially, but not perfectly,
467 compensate for the increase in the wind-driven Deacon Cell. We now see a potential role for an-
468 other type of eddy, the *standing eddy*, at higher resolution than Hallberg and Gnanadesikan (2006),
469 that plays the dominant role in poleward flow rather than transient eddies (Dufour et al. 2012) to
470 counter the wind-driven equatorward circulation.

471 In a coupled model changes in the MOC are connected directly with changes in surface wa-
472 ter mass transformation. This is due to changes in the outcropping position of potential density
473 surfaces and the associated change in surface buoyancy forcing. The water mass analysis is a
474 diagnostic tool showing consistency between the two analysis methods. It is fundamentally prob-
475 lematic to separate wind and buoyancy forcing in a coupled climate model to distinguish relative
476 contributions to changes in the MOC and ACC transport. Ultimately, in this model, the wind is re-
477 sponsible for the changes in the MOC and ACC transport since this is the perturbed variable. Our
478 results suggest a key role for the ocean since changes to SST distributions (Fig. 11c) are accom-
479 panied by changes to surface heating and cooling (Fig. 12c) that dominate the surface buoyancy
480 flux (Fig. 12a).

481 In this study we have simulated a ~ 21 -year perturbation to the Southern Ocean that resolves
482 mesoscale eddies. This simulation pushed the limits of the community's current computational
483 capabilities. Ideally, analyzing the full response of the overturning circulation to a perturbation of

484 this type would require a simulation that is at least an order of magnitude longer. Thus, parame-
485 terization of mesoscale processes is still needed. This simulation, however, does support the study
486 of Thompson and Garabato (2014), which suggests that the equilibration of the ACC to changes
487 in surface wind forcing will principally involve processes that are zonally-asymmetric. A change
488 in the wind stress without an increase in the zonal mean transport requires a greater vertical mo-
489 mentum flux carried out by transient eddies. Thompson and Garabato (2014) argue that changes
490 in eddy activity will be focused in standing meanders related to fluctuations in the amplitude and
491 wavelength of the meander. It is important to note that this response is quite different from the
492 coarse-resolution study of GD11, where the GM coefficient increases almost uniformly through-
493 out the ACC. A key result of this study is that directly resolving mesoscale eddies shows that the
494 response of ACC's EKE, for instance, to changes in wind stress is likely too nuanced to be de-
495 scribed by trends spanning the whole ACC or even basins. We plan to analyze the momentum and
496 vorticity budgets of both high and low resolution simulations, similar to Cronin and Watts (1996)
497 and Hughes (2005) in a future study.

498 There are some potential shortcomings of our simulation. One shortcoming is the shortness of
499 the WP experiment. It is possible that there is decadal variability, but this is not possible to assess
500 in a ~ 21 -year record. Another shortcoming is that the analysis was done using monthly archived
501 data. Ballarotta et al. (2013) found close correspondence in the MOC at 5-day versus monthly
502 archived data, suggesting that most of the signal is at monthly time scales and longer. However,
503 their analysis was done in an eddy-permitting model (0.25°), which does not adequately resolve
504 the first baroclinic deformation radius at these latitudes (Hallberg 2013). Encouragingly, Aber-
505 nathey and Wortham (2015), analyzing the same class of CESM simulation used here, found that
506 mesoscale eddy fluxes were dominated by sub-monthly frequencies. Future studies, for example,

507 could focus on longer simulations, meridional shifts of the mean winds to simulate past climates,
508 and increases in vertical resolution.

509 With these caveats set aside, the high-resolution simulation has shown how increasing winds
510 could lead to an increase in the MOC over the time scales of twenty years. The results from
511 this study broadly agree with ozone depletion experiments, meant to simulate the increase in zonal
512 wind stress in the Southern Hemisphere during austral summer (Ferreira et al. 2015; Solomon et al.
513 2015). The average SST difference during the last ten years of our WP experiment resemble the
514 slow time-scale response in Ferreira et al. (2015), in which there is warming around Antarctica and
515 cooling at mid-latitudes (Fig. 11c). The wind stress changes are stronger in our WP experiment
516 than in the ozone depletion studies and as a result we see much more warming, up to 2°C, in
517 places around Antarctica. These results are indicative of an increase in the lower cell of the MOC
518 (Fig. 8), which causes more upwelling of warm and salty Circumpolar Deep Water (CDW). The
519 upwelling of CDW melts more sea ice throughout the year, which leads to an enhancement of
520 FWFs surrounding Antarctica. The recent trends in winds observed over the past few decades in
521 Southern Hemisphere winds may already be having an influence on the MOC. This would infer
522 that the oceanic uptake of CO₂ may be changing as well.

523 *Acknowledgments.* SPB was supported by the President and Director’s Fund at the California In-
524 stitute of Technology. AFT was supported by NSF grant NSF OCE-1235488. This manuscript was
525 greatly improved by comments from Andy Hogg and an anonymous reviewer. We thank Justin
526 Small for providing the control experiment. Computational resources for the simulation analyzed
527 here was provided by the NCAR Computational and Information Systems Lab under the “Accel-
528 erated Scientific Discovery” program. We also thank Marcus Jochum for helpful comments that

529 improved the manuscript and technical support from Gokhan Danabasoglu. NCAR is supported
530 by the National Science Foundation.

531 **References**

532 Abernathey, R., and P. Cessi, 2014: Topographic enhancement of eddy efficiency in baroclinic
533 equilibration. *Journal of Physical Oceanography*, **44**, 2107–2126.

534 Abernathey, R., J. Marshall, and D. Ferreira, 2011: The dependence of Southern Ocean Meridional
535 Overturning on wind stress. *Journal of Physical Oceanography*, **41**, 2261–2278.

536 Abernathey, R. P., and C. Wortham, 2015: Phase speed cross spectra of eddy heat fluxes in the
537 pacific. *J. Phys. Oceanogr.*, **45**, 1285–1301, doi:10.1175/JPO-D-14-0160.1.

538 Abram, N. J., R. Mulvaney, F. Vimeux, S. J. Phipps, J. Turner, and M. H. England, 2014: Evolution
539 of the Southern Annular Mode during the past millennium. *Nature Climate Change*, **4**, 564–569.

540 Ballarotta, M., S. Drijfhout, T. Kuhlbrodt, and K. Döös, 2013: The residual circulation of the
541 Southern Ocean: Which spatio-temporal scales are needed? *Ocean Modelling*, **64**, 46–55.

542 Bishop, S. P., and F. O. Bryan, 2013: A comparison of mesoscale eddy heat fluxes from obser-
543 vations and a high-resolution ocean model simulation of the Kuroshio Extension. *Journal of*
544 *Physical Oceanography*, **43**, 2563–2570.

545 Böning, C. W., A. Dispert, M. Visbeck, S. R. Rintoul, and F. U. Schwarzkopf, 2008: The response
546 of the Antarctic Circumpolar Current to recent climate change. *Nature Geoscience*, **1**, 864–869.

547 Bryan, F. O., P. R. Gent, and R. Tomas, 2014: Can Southern Ocean eddy effects be parameterized
548 in climate models. *Journal of Climate*, **27**, 411–425.

549 Chidichimo, M. P., K. A. Donohue, D. R. Watts, and K. L. Tracey, 2014: Baroclinic transport time
550 series of the Antarctic Circumpolar Current measured in Drake Passage. *Journal of Physical*
551 *Oceanography*, **44**, 1829–1853.

552 Cronin, M., and D. R. Watts, 1996: Eddy-mean flow interaction in the Gulf Stream at 68°W. Part
553 I: Eddy energetics. *Journal of Physical Oceanography*, **26** (10), 2107–2131.

554 de Szoeke, R. A., and M. D. Levine, 1981: The advective flux of heat by mean geostrophic motions
555 in the Southern Ocean. *Deep Sea Res.*, **28A** (10), 1057–1085.

556 Döös, K., and D. J. Webb, 1994: The Deacon cell and the other meridional cells of the Southern
557 Ocean. *Journal of Physical Oceanography*, **24**, 429–442.

558 Downes, S., A. Gnanadesikan, S. Griffies, and J. Sarmiento, 2011: Water mass exchange in the
559 Southern Ocean in coupled climate models. *Journal of Physical Oceanography*, **41**, 1756–1771.

560 Downes, S. M., and A. M. Hogg, 2013: Southern Ocean circulation and eddy compensation in
561 CMIP5 models. *Journal of Climate*, **26**, 7198–7220.

562 Dufour, C., J. L. Sommer, J. Zika, M. Gehlen, J. Orr, P. Mathiot, and B. Barnier, 2012: Stand-
563 ing and transient eddies in the response of the Southern Ocean Meridional Overturning to the
564 Southern Annular Mode. *Journal of Climate*, **25**, 6958–6974.

565 Farneti, R., and Coauthors, 2015: An assessment of Antarctic Circumpolar Current and Southern
566 Ocean Meridional Overturning Circulation sensitivity during 1958–2007 in a suite of interan-
567 nual CORE-II simulations. *Ocean Modelling*, submitted.

568 Ferreira, D., J. Marshall, C. M. Bitz, S. Solomon, and A. Plumb, 2015: Antarctic ocean and sea ice
569 response to ozone depletion: A two-time-scale problem. *Journal of Climate*, **28**, 1206–1226.

570 Firing, Y. L., T. K. Chereskin, and M. R. Mazloff, 2011: Vertical structure and transport of the
571 Antarctic Circumpolar Current in Drake Passage from direct velocity observations. *Journal of*
572 *Geophysical Research*, **116 (C08015)**, 16, doi:10.1029/2011JC006999.

573 Gent, P., and Coauthors, 2011: The Community Climate System Model version 4. *Journal of*
574 *Climate*, **24**, 4973–4991.

575 Gent, P. R., 2015: Effects of Southern Hemisphere wind changes on the Meridional Overturning
576 Circulation in ocean models. *Annual Review of Marine Science*, submitted.

577 Gent, P. R., and G. Danabasoglu, 2011: Response to increasing southern hemisphere winds in
578 CCSM4. *Journal of Climate*, **24**, 4992–4998.

579 Gent, P. R., and J. C. McWilliams, 1990: Isopycnal mixing in ocean circulating models. *Journal*
580 *of Physical Oceanography*, **20**, 150–155.

581 Gnanadesikan, A., M.-A. Pradal, and R. Abernathey, 2015: Isopycnal mixing by mesoscale ed-
582 dies significantly impacts oceanic anthropogenic carbon uptake. *Geophysical Research Letters*,
583 **42 (11)**, 4249–4255, doi:10.1002/2015GL064100, 2015GL064100.

584 Hallberg, R., 2013: Using a resolution function to regulate parameterizations of oceanic mesoscale
585 eddies. *Ocean Modelling*, **72**, 92–103.

586 Hallberg, R., and A. Gnanadesikan, 2006: The role of eddies in determining the structure and
587 response of wind-driven Southern Hemisphere overturning: Results from the modeling eddies
588 in the Southern Ocean (MESO) project. *Journal of Physical Oceanography*, **36**, 2232–2252.

589 Hogg, A. M., M. P. Meredith, D. P. Chambers, E. P. Abrahamson, C. W. Hughes, and A. K. Mor-
590 rison, 2015: Recent trends in the Southern Ocean eddy field. *Journal of Geophysical Research*,
591 **120**, 257–267, doi:10.1002/2014JC010470.

592 Hughes, C., 2005: Nonlinear vorticity balance of the Antarctic Circumpolar Current. *Journal of*
593 *Geophysical Research*, **110**, C11 008, doi:10.1029/2004JC002753.

594 Hunke, E., and W. Lipscomb, 2008: CICE: the Los Alamos sea ice model user's manual, version
595 4. Tech. rep., Los Alamos National Laboratory.

596 Hurrell, J. W., and Coauthors, 2013: The Community Earth System Model: A framework for
597 collaborative research. *Bulletin of the American Meteorological Society*, **94**, 1339–1360.

598 Iudicone, D., G. Madec, and T. J. McDougall, 2008: Water-mass transformations in a neutral
599 density framework and the key role of light penetration. *J. Phys. Oceanogr.*, **38**, 1357–1376.

600 Johnson, G. C., and H. L. Bryden, 1989: On the size of the Antarctic Circumpolar Current. *Deep*
601 *Sea Res.*, **36**, 39–53.

602 Kirtman, B., and Coauthors, 2012: Impact of ocean model resolution on CCSM climate simula-
603 tions. *Climate Dynamics*, **39**, 1303–1328.

604 Langlais, C. E., S. R. Rintoul, and J. D. Zika, 2015: Sensitivity of Antarctic Circumpolar Cur-
605 rent transport and eddy activity to wind patterns in the Southern Ocean. *Journal of Physical*
606 *Oceanography*, **45**, 1051–1067.

607 Large, W. G., and A. J. G. Nurser, 2001: Ocean surface water mass transformation. *Ocean Circu-*
608 *lation and Climate – Observing and Modelling the Global Ocean*, Academic Press.

609 Large, W. G., and S. G. Yeager, 2009: The global climatology of an interannually varying air-sea
610 flux data set. *Climate Dynamics*, **33**, 341–364.

611 Lawrence, D., and Coauthors, 2011: Parameterization improvements and functional and structural
612 advances in version 4 of the Community Land Model. *Journal of Advances in Modeling Earth*
613 *Systems*, **3** (2011MS000045).

614 Lee, M., and A. Coward, 2003: Eddy mass transport for the Southern Ocean in an eddy-permitting
615 global ocean model. *Ocean Modelling*, **5**, 249–266.

616 Lenn, Y.-D., T. K. Chereskin, J. Sprintall, and J. L. McClean, 2011: Near-surface eddy heat and
617 momentum fluxes in the Antarctic Circumpolar Current in Drake Passage. *Journal of Physical*
618 *Oceanography*, **41**, 1385–1407.

619 Marsh, R., A. J. G. Nurser, A. P. Megann, and A. L. New, 2000: Water mass transformation in the
620 Southern Ocean of a global isopycnal coordinate gcm. *J. Phys. Oceanogr.*, **40**, 1013–1045.

621 Marshall, J., D. Jamous, and J. Nilsson, 1999: Reconciling thermodynamic and dynamic methods
622 of computation of water-mass transformation rates. *Deep Sea Res. I*, **46**, 545–572.

623 Marshall, J., D. Olbers, H. Ross, and D. Wolf-Gladrow, 1993: Potential vorticity constraints on
624 the dynamics and hydrography of the Southern Ocean. *J. Phys. Oceanogr.*, **23**, 465–487.

625 Marshall, J., and T. Radko, 2003: Residual-mean solutions for the Antarctic Circumpolar Current
626 and its associated Overturning Circulation. *Journal of Physical Oceanography*, **33**, 2341–2354.

627 Marshall, J., and K. Speer, 2012: Closure of the meridional overturning circulation through South-
628 ern Ocean upwelling. *Nature Geoscience*, **5**, 171–180.

629 McClean, J., and Coauthors, 2011: A prototype two-decade fully-coupled fine-resolution CCSM
630 simulation. *Ocean Modelling*, doi:doi:10.1016/j.ocemod.2011.02.011.

631 Meredith, M. P., and A. M. Hogg, 2006: Circumpolar response of Southern Ocean eddy activity
632 to a change in the Southern Annular Mode. *Geophysical Research Letters*, **33**, L16 608, doi:
633 10.1029/2006GL026499.

634 Morrison, A. K., T. L. Frölicher, and J. L. Sarmiento, 2015: Upwelling in the Southern Ocean.
635 *Physics Today*, **68**, 27–32.

- 636 Morrison, A. K., and A. M. Hogg, 2013: On the relationship between Southern Ocean Overturning
637 and ACC transport. *Journal of Physical Oceanography*, **43**, 140–148.
- 638 Munday, D. R., H. L. Johnson, and D. P. Marshall, 2013: Eddy saturation of equilibrated circum-
639 polar currents. *Journal of Physical Oceanography*, **43**, 507–532.
- 640 Newsom, E., C. Bitz, F. Bryan, R. P. Abernathey, and P. Gent, 2015: Sea ice processes control
641 abyssal Southern Ocean heat uptake in a fine resolution ocean climate model, manuscript sub-
642 mitted to *Journal of Climate*.
- 643 Nikurashin, M., and G. Vallis, 2012: A theory of the interhemispheric meridional overturning
644 circulation and associated stratification. *J. Phys. Oceanogr.*, **42**, 1652–1667.
- 645 Sallée, J.-B., R. J. Matear, S. R. Rintoul, and A. Lenton, 2012: Localized subduction of anthro-
646 pogenic carbon dioxide in the Southern Hemisphere oceans. *Nature Geoscience*, **5**, 579–584.
- 647 Small, R. J., and Coauthors, 2014: A new high-resolution global climate simulation using Comm-
648 nunity Atmosphere Model version 5. *Journal of Advances in Modeling Earth Systems*, **6**, 1065–
649 1094, doi:10.1002/2014MS000363.
- 650 Smith, K. S., 2007: The geography of linear baroclinic instability in Earth’s oceans. *Journal of*
651 *Marine Research*, **65**, 655–683.
- 652 Solomon, A., L. Polvani, K. Smith, and R. Abernathey, 2015: The impact of ozone depleting
653 substances on the circulation, temperature, and salinity of the Southern Ocean: An attribution
654 study with CESM1 (WACCM). *Geophysical Research Letters*, **42**, 5547–5555, doi:10.1002/
655 2015GL064744.
- 656 Speer, K., and E. Tziperman, 1992: Rates of water mass formation in the North Atlantic Ocean. *J.*
657 *Phys. Oceanogr.*, **22**, 93–104.

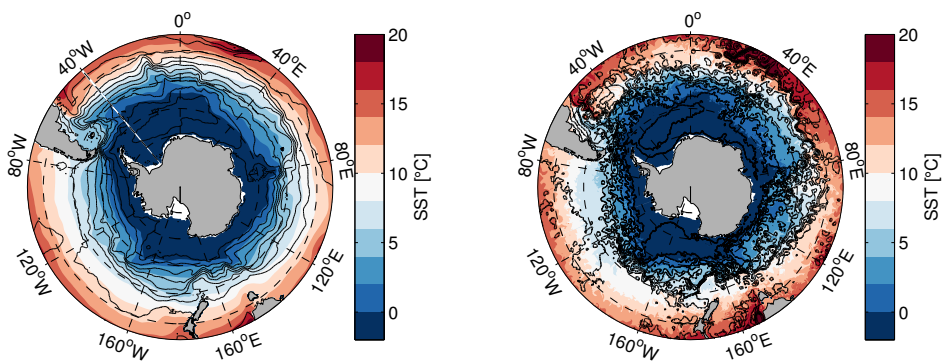
- 658 Stewart, A. L., R. Ferrari, and A. F. Thompson, 2014: On the importance of surface forcing in
659 conceptual models of the deep ocean. *Journal of Physical Oceanography*, **44**, 891–899.
- 660 Straub, D., 1993: On the transport and angular momentum balance of channel models of the
661 Antarctic Circumpolar Current. *Journal of Physical Oceanography*, **23**, 776–782.
- 662 Thompson, A. F., and A. C. N. Garabato, 2014: Equilibration of the Antarctic Circumpolar Current
663 by standing meanders. *Journal of Physical Oceanography*, **44**, 1811–1828.
- 664 Thompson, D. W., S. Solomon, P. J. Kushner, M. H. England, K. M. Grise, and D. J. Karoly, 2011:
665 Signatures of the Antarctic ozone hole in Southern Hemisphere surface climate change. *Nature*
666 *Geoscience*, doi:DOI:10.1038/NGEO1296.
- 667 Toggweiler, J. R., 2009: Shifting Westerlies. *Science*, **323**, 1434–1435.
- 668 Treguier, A. M., and J. C. McWilliams, 1990: Topographic influences on wind-driven, stratified
669 flow in a beta-plane channel: An idealized model for the antarctic circumpolar current. *J. Phys.*
670 *Oceanogr.*, **20** (3), 321–343.
- 671 Treguier, A. M., J. L. Sommer, J. Molines, and B. D. Cuevas, 2010: Response of the Southern
672 Ocean to the Southern Annular Mode: Interannual variability and multidecadal trend. *Journal*
673 *of Physical Oceanography*, **40**, 1659–1668.
- 674 Tziperman, E., 1986: On the role of interior mixing and air-sea fluxes in determining the stratifi-
675 cation and circulation of the oceans. *J. Phys. Oceanogr.*, **16**, 680–693.
- 676 Viebahn, J., and C. Eden, 2012: Standing eddies in the Meridional Overturning Circulation. *Jour-*
677 *nal of Physical Oceanography*, **42**, 1486–1508.
- 678 Volkov, D. L., L.-L. Fu, and T. Lee, 2010: Mechanisms of the meridional heat transport in the
679 Southern Ocean. *Ocean Dynamics*, **60**, 791–801.

- 680 Walin, G., 1982: On the relation between sea-surface heat flow and thermal circulation in the
681 ocean. *Tellus*, **34**, 187–195.
- 682 Ward, M. L., and A. M. Hogg, 2011: Establishment of momentum balance by form stress in a
683 wind-driven channel. *Ocean Modelling*, **40**, 133–146.
- 684 Wolfe, C. L., and P. Cessi, 2010: What sets the strength of the middepth stratification and overturn-
685 ing circulation in eddying ocean models? *Journal of Physical Oceanography*, **40**, 1520–1538.
- 686 Wolff, J.-O., E. Maier-Reimer, and D. J. Olbers, 1991: Wind-driven flow over topography in a
687 zonal beta-plane channel: A quasi-geostrophic model of the Antarctic Circumpolar Current. *J.*
688 *Phys. Oceanogr.*, **21**, 263–291.
- 689 Zika, J. D., J. L. Sommer, C. O. Dufour, A. C. N. Garabato, and A. Blaker, 2013a: Acceleration
690 of the Antarctic Circumpolar Current by wind stress along the coast of Antarctica. *Journal of*
691 *Physical Oceanography*, **43**, 2772–2784.
- 692 Zika, J. D., and Coauthors, 2013b: Vertical eddy fluxes in the Southern Ocean. *Journal of Physical*
693 *Oceanography*, **43**, 941–955.

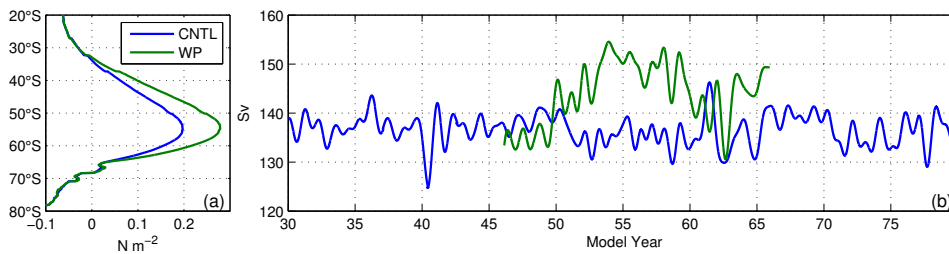
LIST OF FIGURES

695	Fig. 1.	Snapshots of austral winter SST and SSH in low- (1° , left) and high-resolution (0.1° , right) CESM. Color contours are SST ($ci = 1^\circ\text{C}$) and black contours are SSH ($ci = 25\text{ cm}$).	35
696			
697	Fig. 2.	(a) Time and zonal mean zonal wind stress for the control and WP experiments for model year 56–66. (b) One-year low-pass filtered times series of Drake Passage transport using a fourth-order Butterworth filter centered around model years 45–66. The first and last year of each time series was removed due to Gibbs ringing at the end points.	36
698			
699			
700			
701	Fig. 3.	Southern Ocean monthly time averaged and area-averaged (south of 30°S) ocean temperature at 2889 m depth for the control and WP simulations.	37
702			
703	Fig. 4.	(a) Area-average time series of daily surface EKE anomaly referenced to the control mean derived from daily SSH. (b) 10-year linear trend in EKE for model years 45–56 in the WP experiment (color contours, $ci = 50\text{ cm}^2\text{ s}^{-2}\text{ decade}^{-1}$). For reference to the ACC, light gray contours are the mean SSH ($ci = 25\text{ cm}$) for the WP experiment.	38
704			
705			
706			
707	Fig. 5.	Change in upper 1000 m vertically-averaged EKE (WP minus CNTL) for model years 56–66. Color contours have $ci = 50\text{ cm}^2\text{ s}^{-2}$ and thin black contours are where the change in EKE is zero. The thick black (CNTL) and magenta (WP) contours are the -150 and -25 cm mean SSH contours that pass through Drake Passage.	39
708			
709			
710			
711	Fig. 6.	Differences between the time and zonal mean σ_2 (WP-CNTL) for model years 56–66. (a) Full water column. Color contours are the differences with $ci = 0.01\text{ kg m}^{-3}$. (b) Same as in (a), but for the upper ocean. The black and gray contours in both are the depth of the time and zonal mean σ_2 surfaces in the control and WP simulations respectively with $ci = 0.25\text{ kg m}^{-3}$. (c) Probability density distribution for potential density differences.	40
712			
713			
714			
715			
716	Fig. 7.	The Eulerian-mean MOC (Eq. 1) for the control (a), WP (b), and difference (c). The color contours are the overturning streamfunction in units of Sv with $ci = 2\text{ Sv}$ for (a) and (b) and $ci = 1\text{ Sv}$ for (c). The black and gray contours are the depth of the time and zonal mean σ_2 surfaces in the control and WP simulations respectively with $ci = 0.25\text{ kg m}^{-3}$	41
717			
718			
719			
720	Fig. 8.	MOC (ψ_{moc} , a–c), mean overturning circulation ($\bar{\psi}$, d–f), and transient eddy overturning circulation (ψ^* , g–i) for the control (left column), WP (middle column), and difference (right column, WP minus control). Color contours have $ci = 1\text{ Sv}$. Black and gray contours are positive and negative overturning circulation respectively with $ci = 5\text{ Sv}$	42
721			
722			
723			
724	Fig. 9.	Mean overturning circulation, $\bar{\psi}$, decomposed into the time and zonal mean, $[\bar{\psi}]$, and standing, ψ^\dagger , overturning circulation. Mean overturning (a–c, same as d–f in Fig. 8), time and zonal mean overturning (d–f), and standing overturning circulation (g–i) for the control (left column), WP (middle column), and difference (right column, WP minus control). Color contours have $ci = 1\text{ Sv}$. Black and gray contours are positive and negative overturning circulation respectively with $ci = 5\text{ Sv}$	43
725			
726			
727			
728			
729			
730	Fig. 10.	The change in the time and zonal mean kinetic energy (Eq. 10) between the WP and control simulations for model years 56–66.	44
731			
732	Fig. 11.	Sea surface density, temperature, and salinity differences (WP minus control) for model years 56–66. (a) Density difference (color contours, $ci = 0.05\text{ kg m}^{-3}$), (b) Zonal average surface density, (c) SST color contours ($ci = 0.25\text{ }^\circ\text{C}$), (d) Zonal average SST, (e) Salinity	
733			
734			

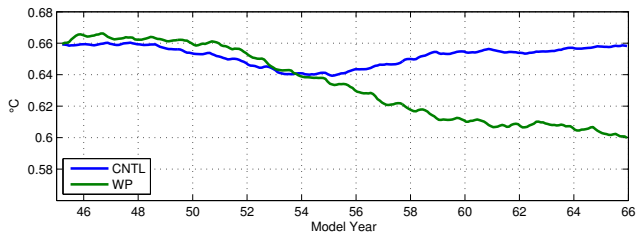
735	differences ($ci = 0.1 \text{ g kg}^{-1}$), and (f) Zonal average salinity. Black (positive) and gray	
736	(negative) contours ($ci = 10 \text{ cm}$) are the change in mean SSH.	45
737	Fig. 12. Surface buoyancy flux differences between the control and WP experiments for model years	
738	56–66. The sign convention of negative means the ocean is cooling or becoming saltier. (a)	
739	is total surface buoyancy and panels (c) and (e) are contributions from heat and fresh water	
740	fluxes respectively ($ci = 0.25 \times 10^{-8} \text{ m}^2 \text{ s}^{-3}$). The zonally-averaged total surface buoyancy,	
741	heat, and fresh water flux contributions are (b), (d), and (f) respectively. Black (positive) and	
742	gray (negative) contours ($ci = 10 \text{ cm}$) are the change in mean SSH.	46
743	Fig. 13. Sea ice thickness difference (WP minus control) for model years 56–66. (a) JFM (January,	
744	February, March) and (b) JAS (July, August, September) difference ($ci = 0.1 \text{ m}$).	47
745	Fig. 14. Surface water mass transformation in control (solid) and perturbation (dashed) experiments.	
746	The heat-flux-driven transformation is in red, the freshwater-flux-driven transformation is in	
747	blue, and the net transformation is in black. Positive values mean indicate water being made	
748	denser.	48



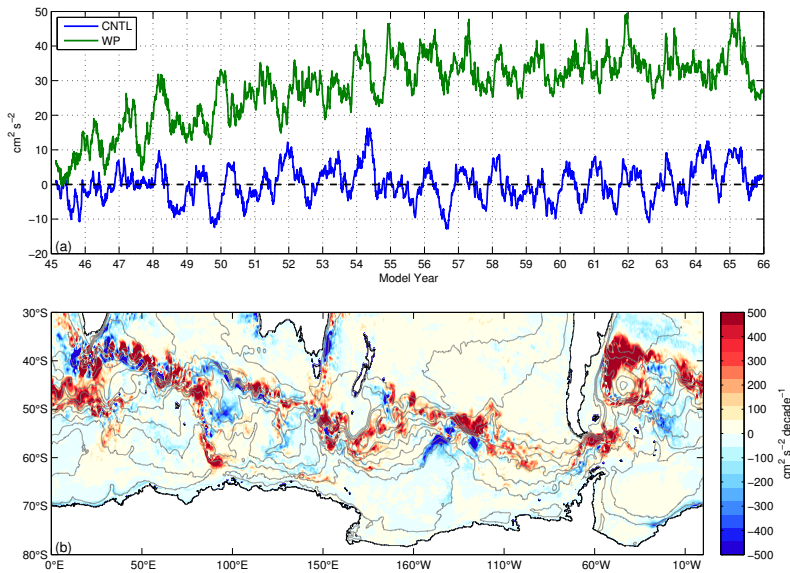
749 FIG. 1. Snapshots of austral winter SST and SSH in low- (1° , left) and high-resolution (0.1° , right) CESM.
 750 Color contours are SST ($ci = 1^\circ\text{C}$) and black contours are SSH ($ci = 25\text{ cm}$).



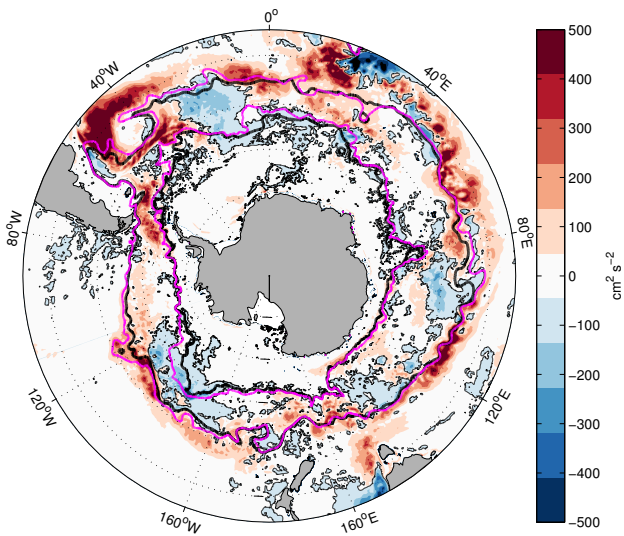
751 FIG. 2. (a) Time and zonal mean zonal wind stress for the control and WP experiments for model year 56–
 752 66. (b) One-year low-pass filtered times series of Drake Passage transport using a fourth-order Butterworth filter
 753 centered around model years 45–66. The first and last year of each time series was removed due to Gibbs ringing
 754 at the end points.



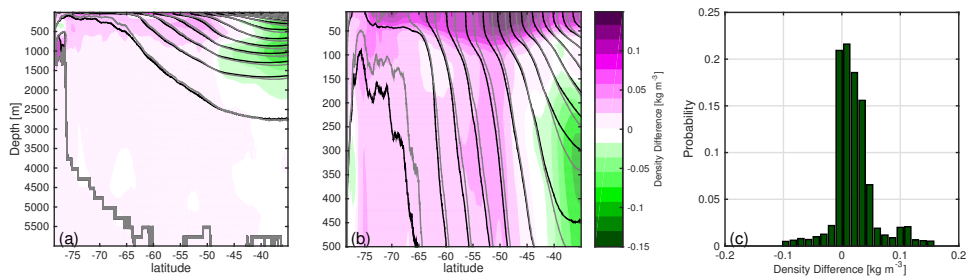
755 FIG. 3. Southern Ocean monthly time averaged and area-averaged (south of 30°S) ocean temperature at 2889
756 m depth for the control and WP simulations.



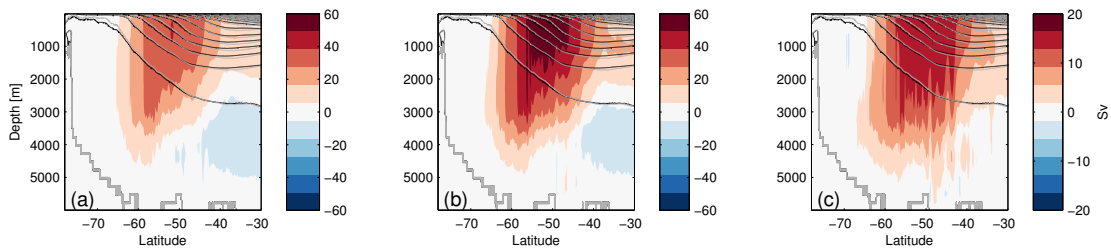
757 FIG. 4. (a) Area-average time series of daily surface EKE anomaly referenced to the control mean derived
 758 from daily SSH. (b) 10-year linear trend in EKE for model years 45–56 in the WP experiment (color contours,
 759 $ci = 50 \text{ cm}^2 \text{ s}^{-2} \text{ decade}^{-1}$). For reference to the ACC, light gray contours are the mean SSH ($ci = 25 \text{ cm}$) for the
 760 WP experiment.



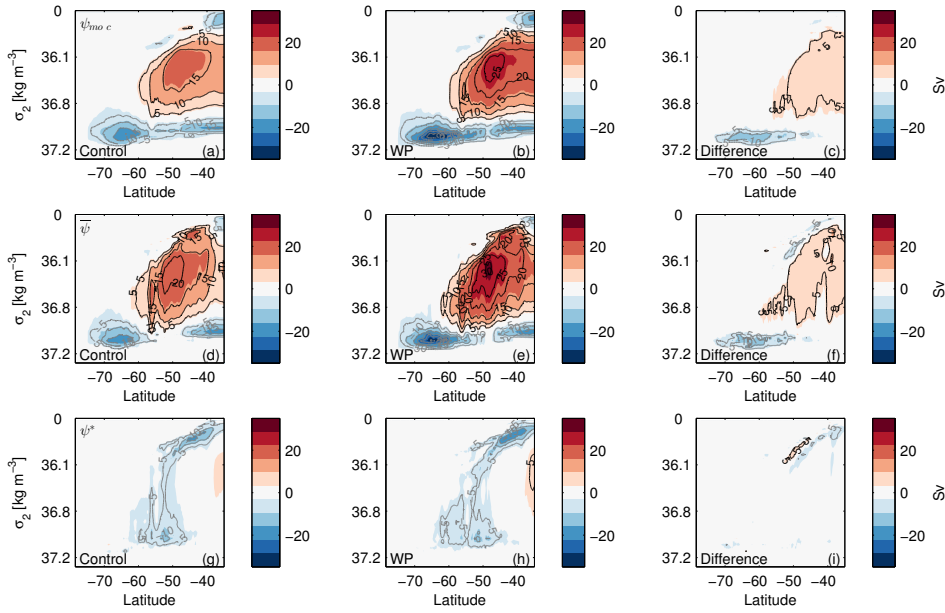
761 FIG. 5. Change in upper 1000 m vertically-averaged EKE (WP minus CNTL) for model years 56–66. Color
 762 contours have $c_i = 50 \text{ cm}^2 \text{ s}^{-2}$ and thin black contours are where the change in EKE is zero. The thick black
 763 (CNTL) and magenta (WP) contours are the -150 and -25 cm mean SSH contours that pass through Drake
 764 Passage.



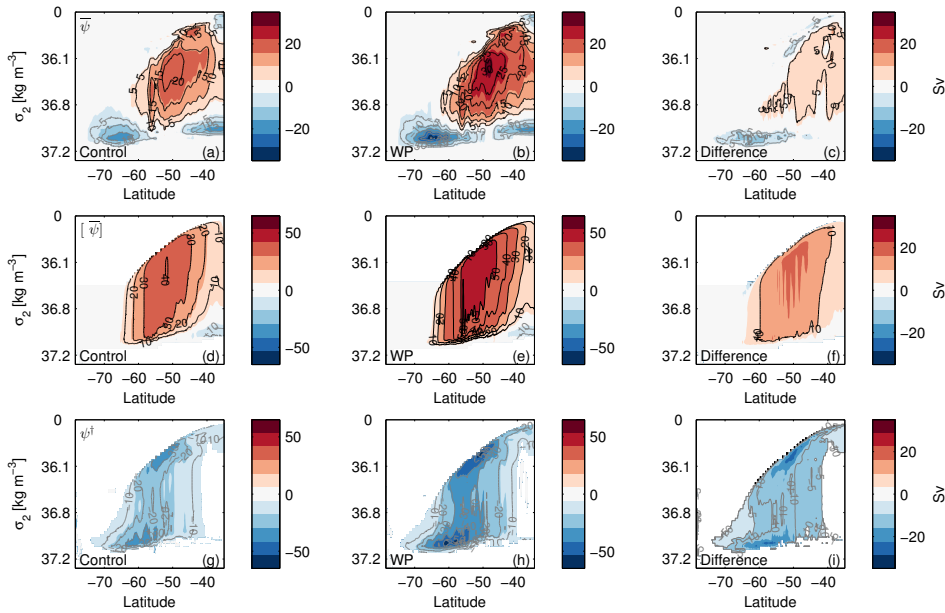
765 FIG. 6. Differences between the time and zonal mean σ_2 (WP-CNTL) for model years 56–66. (a) Full water
 766 column. Color contours are the differences with $c_i = 0.01 \text{ kg m}^{-3}$. (b) Same as in (a), but for the upper ocean.
 767 The black and gray contours in both are the depth of the time and zonal mean σ_2 surfaces in the control and
 768 WP simulations respectively with $c_i = 0.25 \text{ kg m}^{-3}$. (c) Probability density distribution for potential density
 769 differences.



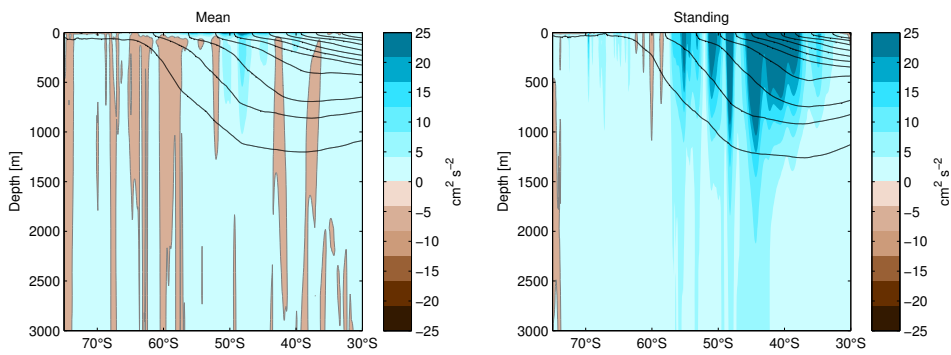
770 FIG. 7. The Eulerian-mean MOC (Eq. 1) for the control (a), WP (b), and difference (c). The color contours
 771 are the overturning streamfunction in units of Sv with $c_i = 2$ Sv for (a) and (b) and $c_i = 1$ Sv for (c). The
 772 black and gray contours are the depth of the time and zonal mean σ_2 surfaces in the control and WP simulations
 773 respectively with $c_i = 0.25 \text{ kg m}^{-3}$.



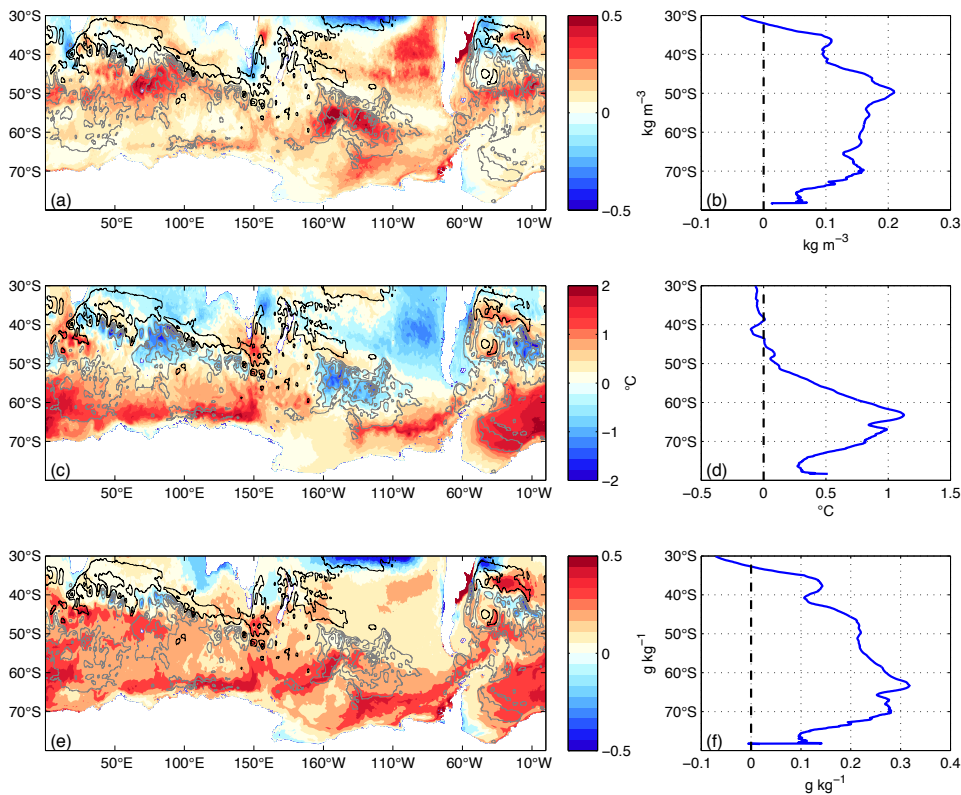
774 FIG. 8. MOC (ψ_{moc} , a–c), mean overturning circulation ($\bar{\psi}$, d–f), and transient eddy overturning circulation
 775 (ψ^* , g–i) for the control (left column), WP (middle column), and difference (right column, WP minus control). Color contours have $ci = 1$ Sv. Black and gray contours are positive and negative overturning circulation
 776 respectively with $ci = 5$ Sv.
 777



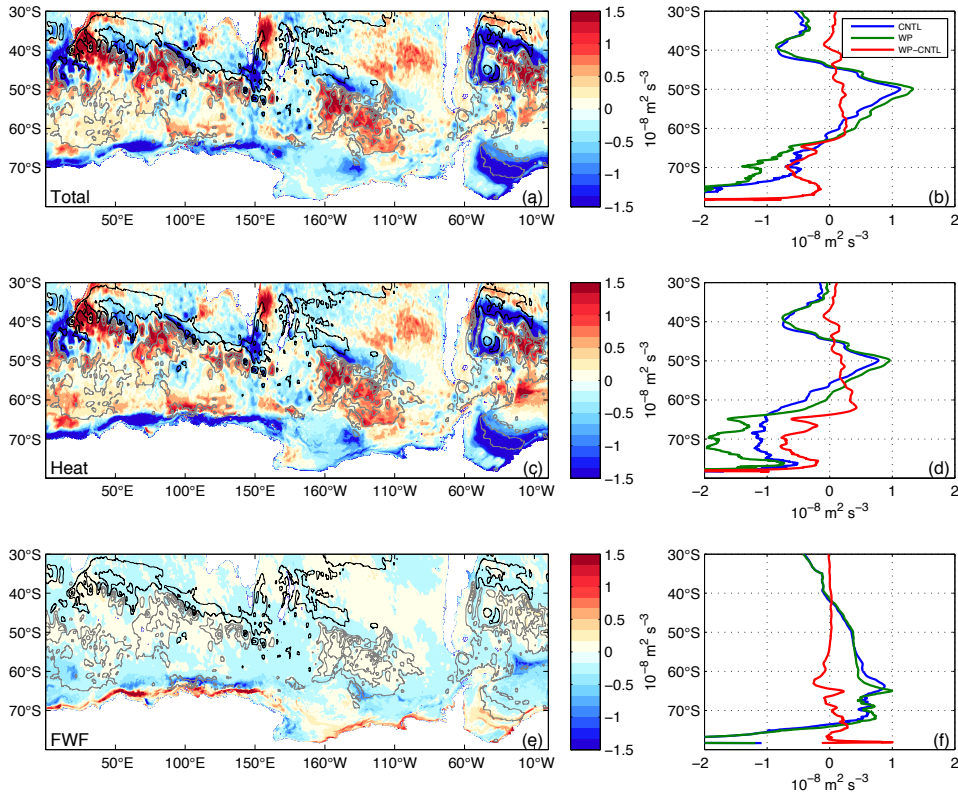
778 FIG. 9. Mean overturning circulation, $\overline{\psi}$, decomposed into the time and zonal mean, $[\overline{\psi}]$, and standing, ψ^\dagger ,
 779 overturning circulation. Mean overturning (a–c, same as d–f in Fig. 8), time and zonal mean overturning (d–f),
 780 and standing overturning circulation (g–i) for the control (left column), WP (middle column), and difference
 781 (right column, WP minus control). Color contours have $ci = 1$ Sv. Black and gray contours are positive and
 782 negative overturning circulation respectively with $ci = 5$ Sv.



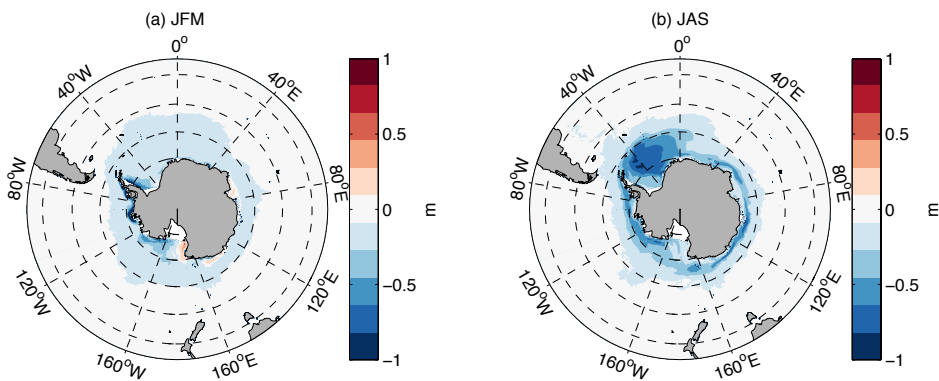
783 FIG. 10. The change in the time and zonal mean kinetic energy (Eq. 10) between the WP and control
 784 simulations for model years 56–66.



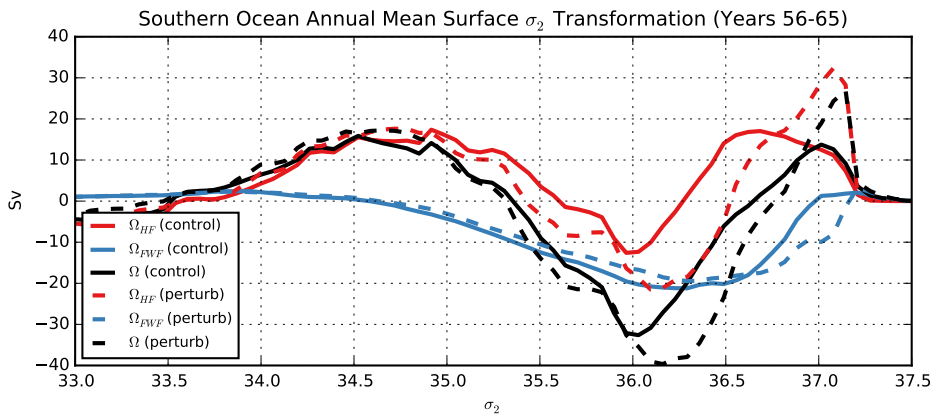
785 FIG. 11. Sea surface density, temperature, and salinity differences (WP minus control) for model years 56–
 786 66. (a) Density difference (color contours, $ci = 0.05 \text{ kg m}^{-3}$), (b) Zonal average surface density, (c) SST color
 787 contours ($ci = 0.25 \text{ }^\circ\text{C}$), (d) Zonal average SST, (e) Salinity differences ($ci = 0.1 \text{ g kg}^{-1}$), and (f) Zonal average
 788 salinity. Black (positive) and gray (negative) contours ($ci = 10 \text{ cm}$) are the change in mean SSH.



789 FIG. 12. Surface buoyancy flux differences between the control and WP experiments for model years 56–66.
 790 The sign convention of negative means the ocean is cooling or becoming saltier. (a) is total surface buoyancy and
 791 panels (c) and (e) are contributions from heat and fresh water fluxes respectively ($c_i = 0.25 \times 10^{-8} \text{ m}^2 \text{ s}^{-3}$). The
 792 zonally-averaged total surface buoyancy, heat, and fresh water flux contributions are (b), (d), and (f) respectively.
 793 Black (positive) and gray (negative) contours ($c_i = 10 \text{ cm}$) are the change in mean SSH.



794 FIG. 13. Sea ice thickness difference (WP minus control) for model years 56–66. (a) JFM (January, February,
 795 March) and (b) JAS (July, August, September) difference ($c_i = 0.1$ m).



796 FIG. 14. Surface water mass transformation in control (solid) and perturbation (dashed) experiments. The
 797 heat-flux-driven transformation is in red, the freshwater-flux-driven transformation is in blue, and the trans-
 798 formation is in black. Positive values mean indicate water being made denser.